Journal of the European Ceramic Society 46 (2026) 118706

Contents lists available at ScienceDirect

Journal of the European Ceramic Society

journal homepage: www.elsevier.com/locate/jeurceramsoc

Achieving low friction at high temperature through high-entropy oxide coatings for extreme environments

Ikshita Chaturvedi [a,*], Payank Patel [a], Hamideh Vakilifard [a], Fadhel Ben Ettouil [a], Martin Dienwiebel [b,c], Christian Moreau [a], Pantcho Stoyanov [d]

[a] Department of Mechanical, Industrial and Aerospace Engineering, Concordia University, Canada
[b] Karlsruhe Institute of Technology KIT, Institute for Applied Materials, MicroTribology Center μTC, Strasse Am Forum 5, Karlsruhe 76131, Germany
[c] Fraunhofer-Institute for Mechanics of Materials IWM, MicroTribology Center μTC, Woehlerstrasse 11, Freiburg 79108, Germany
[d] Department of Chemical and Materials Engineering, Concordia University, Canada

ARTICLE INFO

Keywords:
Fretting
High entropy oxides (HEOs)
Friction and wear
Suspension plasma spray (SPS)
Tribology

ABSTRACT

Conventional Ni- and Co-based aerospace alloys continue to face tribological challenges at elevated temperatures, including frictional losses, oxidation-assisted damage, and wear degradation. High-entropy oxides (HEOs), as a class of high-entropy ceramics, offer a promising pathway for developing thermally stable protective coatings for extreme environments where conventional surface materials and lubricants can degrade. In this study, a suspension plasma-sprayed (SPS) $(Y_{0.2}Nd_{0.2}Gd_{0.2}Sm_{0.2}Dy_{0.2})_2Zr_2O_7$ HEO topcoat deposited on an IN625 substrate with an Amdry 386–2.5 bond coat was evaluated under high-temperature fretting against a SiC counterface. The novelty of this work lies in investigating the fretting response of an SPS-deposited rare-earth zirconate HEO coating at 600 °C and 800 °C, where limited studies have addressed the combined effects of temperature, fretting motion, third-body formation, and coating damage evolution in high-entropy ceramic coating systems. The coating showed competitive low-friction behaviour compared with conventional high-temperature metallic alloys and several reported ceramic-based tribological coatings, reaching steady-state coefficients of friction of approximately 0.1 at 600 °C and 0.25 at 800 °C. At 600 °C, the low and stable friction response was associated with the formation and retention of fine oxide-rich third-body debris, resulting in a shallow wear depth of approximately 7 μm. At 800 °C, the coefficient of friction remained relatively low but became more unstable, while the wear depth increased to approximately 43 μm. SEM/EDS and FIB analyses revealed microcracking, chipping, pull-out features, and debris accumulation, indicating reduced tribolayer stability and increased damage accumulation at the higher temperature. Overall, this study highlights the potential of HEOs within the broader family of high-entropy ceramics for high-temperature fretting applications, while also showing that wear resistance is strongly governed by temperature-dependent adhesion, debris stability, and fracture processes.

Summary of Novel Conclusions.

This study investigates the high-temperature fretting behaviour of a suspension plasma-sprayed high-entropy oxide coating, $(Y_{0.2}Nd_{0.2}Gd_{0.2}Sm_{0.2}Dy_{0.2})_2Zr_2O_7$, against a SiC counterface. The novelty lies in evaluating an SPS-deposited high-entropy rare-earth zirconate coating within the broader family of high-entropy ceramic coatings under fretting conditions at 600 °C and 800 °C. Although the starting suspension had a pyrochlore structure, the as-deposited coating transformed into a defect-fluorite structure after SPS processing. Unlike previous studies that mainly focus on high-entropy oxides for thermal barrier applications or high-entropy coatings under conventional sliding, this work identifies the temperature-dependent transition in fretting response from stable third-body-assisted low friction at 600 °C to adhesion- and fracture-assisted wear at 800 °C.

The coating exhibited a dense and relatively uniform microstructure with interspersed vertical cracks. At 600 °C, the coating showed better tribological performance, with a low coefficient of friction of approximately 0.1 and a shallow wear depth of about 7 μm. This behaviour was associated with the formation and retention of oxide-rich debris within the contact, which acted as a

* Corresponding author.
E-mail addresses: ikshita.chaturvedi@mail.concordia.ca (I. Chaturvedi), payank.patel@concordia.ca (P. Patel), pantcho.stoyanov@concordia.ca (P. Stoyanov).

https://doi.org/10.1016/j.jeurceramsoc.2026.118706
Received 1 April 2026; Received in revised form 12 July 2026; Accepted 19 July 2026
Available online 20 July 2026

third body and helped reduce direct interaction between the coating and counterface. The pre-existing vertical cracks did not develop into severe chipping or secondary cracking under this condition. In contrast, at 800 °C, the coefficient of friction remained below approximately 0.3, but the wear depth increased significantly to about 43 μm. The worn surface showed stronger evidence of adhesion, micro-cracking, pull-out, localized chipping, and coating transfer to the counterface. Overall, the study shows that while the SPS-deposited HEO coating can maintain relatively low friction at elevated temperatures, its wear resistance is strongly governed by temperature-dependent debris stability, adhesion, and fracture processes.

1. Introduction

Next-generation aero gas turbines continue to push the boundaries of higher temperatures, pressure ratios, and power densities to improve efficiency and reduce emissions. This also intensifies friction and wear challenges at critical interfaces, such as blades, disks, dovetails, shrouds, rubbing surfaces, splines, fasteners, and bearing-related contacts [1]. Conventional binary and ternary Ni- and Co-based alloys, which are widely used in the aerospace industry, have demonstrated certain performance limitations under demanding operating conditions [2,3]. Therefore, the search for materials capable of operating under severe thermo-mechanical and tribological conditions has led to growing interest in high entropy material systems.

The concept was first introduced through high-entropy alloys [4,5], where several principal elements are combined in comparable amounts rather than relying on a single dominant base element. The similar concept has now been extended to include alloys, carbides, nitrides, borides, silicides, and oxides [6–9]. This broader family of materials offers a large compositional design space, where phase stability, hardness, oxidation resistance, thermal stability, and wear response can be tailored through multi-component chemistry and lattice disorder. The formation of single-phase high-entropy carbides, high-entropy diborides, and entropy-stabilized oxides has demonstrated that configurational disorder can be extended successfully to several ceramic crystal structures, not only metallic solid solutions [10-13]. This is important for high-temperature contact applications, where metallic systems may undergo oxidation-assisted degradation during sliding or fretting [14-17]. Therefore, high-entropy ceramic coatings are attractive for harsh contact environments because they combine ceramic-like hardness and thermal stability with the chemical tunability of high-entropy design.

High-entropy carbides and diborides have been investigated as ultra-high-temperature ceramics because of their high melting points, phase stability, and mechanical robustness. High-entropy nitrides and carbonitrides have also shown promising hardness, adhesion, and wear resistance, making them relevant for protective coating applications [10,18-20]. However, their performance in high-temperature fretting contacts in air is not governed by hardness alone. Under oxidizing sliding conditions, these non-oxide ceramics can undergo surface oxidation, oxide-layer growth, cracking, and debris formation [21,22]. Their friction and wear response may therefore depend on the stability of the oxide layer formed during contact. In addition, very hard ceramic debris can promote abrasive damage if it is not effectively accommodated within the interface. Recent studies on high-entropy carbides and diborides also show that oxidation resistance remains composition-dependent and is often controlled by the formation of protective oxide scales [23-25]. This creates a need to explore oxide-based high-entropy coatings that are chemically stable in oxidizing environments from the beginning of contact.

High-entropy oxides (HEO) provide such a route. Unlike metallic alloys or non-oxide ceramics, HEOs are already chemically complex oxide systems, where several cations are incorporated within a common oxide lattice [12,26]. Therefore, their high-temperature response might not rely primarily on the in-situ formation of an oxide scale during sliding. This is especially relevant for high-temperature fretting in air, where chemical stability, thermal compatibility, and resistance to degradation are required. HEOs are single phase solid solutions that contain five or more cation species. Here, the high configurational entropy contributes to phase stability, while multi cation nature and lattice-distortion effects enable combinations of properties that are difficult to achieve otherwise [27]. Recent studies have shown that HEOs with pyrochlore [28], fluorite, perovskite, and multiphase structures can exhibit low thermal conductivity, tunable thermal expansion, sluggish sintering, and excellent high-temperature phase stability [28-31]. These properties are attractive for high-temperature protective coatings because the surface must remain stable during thermal cycling, oxidation, and mechanical contact. This has already prompted their investigation as thermal barrier coating (TBC) topcoats on turbine components [32-35].

These same characteristics could also potentially be beneficial for tribological coatings in gas-turbine environments. However, their friction and wear response is still much less explored than their thermal barrier behavior. Recent studies have begun to examine the elevated-temperature tribological performance of HEO and related high-entropy ceramic coatings [21,32,36]. However, many of these studies rely on pin-on-disc or reciprocating sliding tests with relatively large stroke lengths, moderate contact pressures, simplified counterface materials, and a single or narrow temperature range [32,36,37]. Therefore, limited information is available on how HEO coatings behave under service-relevant high-temperature fretting conditions. This is particularly important for gas-turbine contacts involving small-amplitude motion, high contact stress, oxidizing atmospheres, and ceramic interfaces such as SiC-based CMC components. As gas turbine architectures continue to incorporate more CMC components and operate at higher temperatures, it becomes important to investigate whether HEO coatings can provide a low-friction protective response across such interfaces.

The novelty of the present work lies in examining an SPS-deposited high-entropy rare-earth zirconate coating, $(Y_{0.2}Nd_{0.2}Gd_{0.2}Sm_{0.2}Dy_{0.2})_2Zr_2O_7$, under high-temperature fretting against a SiC counterface. Previous high-entropy coating studies have largely focused on metallic HEA coatings [8], thin-film high-entropy ceramic systems, or rare-earth zirconate HEOs developed primarily for thermal barrier coating functionality [27]. In this study, controlled high-temperature fretting experiments were employed to investigate friction evolution, wear morphology, and debris formation over temperature ranges relevant to hot-section contacts (e.g., 600–800 °C). Post-test microstructural and chemical characterization was performed to elucidate the underlying wear mechanisms and to relate these to the observed friction and wear responses subsequently.

2. Experimental procedure

2.1. Powder synthesis

A bond coat of composition Ni−22Co−17Cr−12Al−0.5Hf−0.5Y−0.4Si (Amdry 386–2.5, Oerlikon Metco) was applied with a nominal particle size (D50) of 37.9 μm using the HVOF process as discussed here [34]. In addition, HEO with the chemical formula $(Y_{0.2}Nd_{0.2}Gd_{0.2}Sm_{0.2}Dy_{0.2})_2Zr_2O_7$ was synthesized using the solid-state reaction technique. High purity rare rare-earth oxide powders (C99.9%, by Stanford Advanced Materials) of Y_2O_3, Nd_2O_3, Gd_2O_3, Sm_2O_3, Dy_2O_3, and ZrO_2, with particle sizes ranging from 2 to 10 μm, were measured in stoichiometric ratios, homogenized via ball milling (PQ-N2 Planetary Ball Mill, Across International), and subjected to heat treatment in air at 1500 °C for 25 h. The resultant powder displayed a pyrochlore crystal structure. After the heat treatment, the powders were ball-milled (PQ-N2 Planetary Ball Mill, Across International) for an

additional 10 h to reduce particle size to make the suspension for suspension plasma spraying (SPS), as reported elsewhere [34].

2.2. Coating deposition

Ni-based superalloy (IN625) measuring 5.4 cm in diameter and 0.5 cm in thickness (High Performance Alloys Inc., USA) was utilized as a substrate. Before coating, the substrates were grit blasted with alumina (Al_2O_3) to achieve a line roughness of 6 ± 0.5 μm (Ra) and subsequently ultrasonically cleaned in acetone. Line roughness was quantified using a Mitutoyo SJ−210 profilometer (Japan) with a 2.5 mm cutoff length. A minimum of ten measurements was recorded for each sample, and the average Ra value was documented.

To remove residual moisture, HEO powder was dried for 24 h before preparing the suspension. Each suspension was formulated in 99.99% pure anhydrous ethanol, with a solid loading of 10 wt% and 1 wt% polyvinylpyrrolidone (PVP) (Sigma-Aldrich) as a surfactant. The mean particle size (D50) of the HEO powder was 0.9 μm as determined by Spraytec laser diffraction analysis.

The total coating system thickness, including the bond coat and HEO topcoat, was ~350 ± 5 μm, while the HEO topcoat thickness was approximately 195 μm. Before deposition, the substrates were preheated to approximately 400 °C using the plasma torch. As discussed by Vakilifard et al. [34]. A 100 μm bond coat was applied using a high-velocity oxy-fuel (HVOF) process utilizing a Diamond Jet™ 2700 gun (Oerlikon Metco). Table 1 presents an overview of the spray parameters used for the bond coat production. The HEO topcoat was deposited via SPS. Ceramic coatings were sprayed with a Mettech Axial III torch (Northwest Mettech Corp., Surrey, BC, Canada), which has three converging plasma jets generated by separate cathode-anode pairs, together with axial injection of the suspension into the core of the plasma plume. A NanoFeed 350 liquid feeder (Northwest Mettech Corp., Surrey, BC, Canada) was employed for continuous suspension injection. The parameters for the SPS-sprayed HEO are presented in Table 2. Additional information on both HVOF and SPS processes can be found in the authors' previous work [34].

The in-flight particle velocity and temperature were recorded using Accuraspray diagnostic system (Tecnar Automation Ltée, Saint-Bruno, QC, Canada). The errors given in the table represent standard deviations from three independent measurements. [34].

2.3. Coating characterization

Differential scanning calorimetry (DSC) was carried out on the as-sprayed coatings in air with a heating rate of 10 K/min over the temperature range of 25 °C−800 °C, using a Steline DSC + (Setaram KEP Technologies, Geneva, Switzerland). Raman spectroscopy and mapping were conducted with an InVia Reflex Raman microscope (Renishaw plc., UK) using a 532 nm excitation wavelength and a laser power of 50 mW (100%). A 100 × lens was used, yielding a spot size of approximately 1 μm. Each spectrum was acquired with an integration time of 2 s, consisting of two accumulations of 1 s each. Raman maps were collected over a 20 × 20 μm area with 20 points per line, giving a total of 400 spectra per map.

X-ray diffraction (XRD) analysis was carried out on the initial feedstock powders, and after spraying using a Bruker D8 Advance diffractometer (Bruker, Billerica, MA, USA) equipped with a Cu source ($\lambda = 1.5418$ Å), operating at 40 kV and 40 mA. Data were collected over a 2θ range of 20°−70° with a step size of 0.02° and an integration time of 1 s per step. The Vickers microhardness testing was performed on a polished cross section of the coating. The microhardness testing equipment (Multitoya, Japan) was used. Employing a Vickers indenter with 100 gf of applied load. Indentations were placed within the topcoat while avoiding pores, cracks, and interfacial regions. A minimum of 10 valid indentations was used to measure the mean microhardness and standard deviation. Indents were spaced approximately five times the indenter size to avoid the overlapping of affected zones, as reported here [34].

Table 1
Spray parameters for HVOF-sprayed MCrAlY (Amdry 386–2.5) bond coat.

Parameters	Values
Air pressure, kPa	690
Air flow rate, NLPM	446
Propylene pressure, kPa	690
Propylene flow rate, NLPM	102
Oxygen pressure, kPa	1035
Oxygen flow rate, NLPM	183
Carrier gas flow rate, NLPM	14
Powder feed rate, g/min	50
Spray distance, mm	225
Torch traverse speed, mm/s	1000

Table 2
Spray parameters for SPS sprayed HEO ($(Y_{0.2}Nd_{0.2}Gd_{0.2}Sm_{0.2}Dy_{0.2})_2Zr_2O_7$) topcoat.

Spray Parameters	Values
Plasma gas composition (Ar/N2/H2), %	60/20/20
Plasma gas flow, L/min	300
Arc Current, A	220
Electrical power, kW	115
Plasma enthalpy, kJ/L	10.6
Suspension feed rate, mL/min	45
Atomizing gas flow, L/min	15
Standoff distance, mm	100
Torch traverse speed, mm/s	1000
Substrate Temperature, °C	400
Particle Velocity, m/s	592 ± 24
In-Flight Particle Temperature, °C	3404 ± 142
Deposition Efficiency, %	25 ± 5

2.4. Tribological testing and post test characterization

High-temperature fretting tests were performed using a Bruker UMT TriboLab TL, high-temperature chamber in a ball-on-flat configuration, following ASTM G204 with modifications for elevated temperatures. Before testing, the samples were ground with #320, #500, and #800 grit paper, followed by polishing with 9 μm, 3 μm, and 1 μm polishing pads, respectively. The final surface roughness achieved was < 1 μm for all the samples. A SiC ball (10 mm diameter) was used against the flat specimen under a normal load of 15 N and other testing parameters as noted in Table 3. SiC was selected as the counterface to represent a hard, high-temperature ceramic counterbody relevant to advanced gas-turbine material systems. Consequently, SiC/SiC ceramic matrix composites and ceramic barrier coatings are increasingly used or are currently being considered for hot-section components. Not only that, but ceramic barrier coatings are also considered essential for protecting SiC-based components under harsh combustion conditions [38]. In addition, SiC is widely recognized as a high-hardness, high-stiffness, chemically resistant, and wear-resistant ceramic suitable for tribological

Table 3
The Fretting test parameters of the ball on flat tribometer.

Parameters	Values
Counterface	SiC
Counterface Hardness, HV	2500–2800
Frequency, Hz	60
Track Length, μm	300
Velocity, mm/s (avg sliding speed)	36
Load, N	15
Temperature, °C	600 and 800
Cycles	200,000
Surface Roughness, μm	< 1

applications [39]. Therefore, SiC provides a relevant and stable ceramic counterface while minimizing complications associated with metallic counterfaces, such as softening, oxidation, and adhesive metal transfer at 600 °C−800 °C. This allows the observed friction and wear response to be correlated more directly with the HEO coating and the stability of its wear debris/tribolayer. The use of SiC is also consistent with recent high-temperature fretting studies that used SiC as a ceramic counterface to simulate gas-turbine-relevant tribological interfaces [40]. Tests were conducted at 600 °C and 800 °C under dry conditions in air within a covered high-temperature chamber (with an atmosphere not actively controlled). Before sliding, the samples (substrate/coating) were heated to achieve a surface temperature of 600 °C and 800 °C, as measured by a thermocouple on the surface. The specimens were held at the target temperature for 20 min to stabilize the thermal condition. The two temperature ranges were chosen to represent practically relevant and mechanistically distinct regimes for high-temperature fretting regimes rather than to fully map the transition over the entire temperature range, based on the published literature [41,42]. Fretting wear in gas turbine components is commonly associated with high-temperature cyclic micro-slip contacts, and temperatures in the several-hundred-degree range are frequently used to reproduce these conditions in laboratory studies [43]. A lower temperature of 600 °C was chosen as an entry point into the high-temperature fretting behaviour, where oxide-rich third--body formation and retention can begin to influence friction and wear. This temperature is also relevant as conventional solid lubricants such as graphite become increasingly limited in air due to oxidation at elevated temperatures, with oxidation reported to begin around 400 °C and CO/CO_2 formation becoming significant above 500 °C [44]. A higher temperature of 800 °C was chosen to investigate the stability of oxide/third-body tribolayer and the coating's mechanical integrity under more severe thermal-cyclic shear conditions [45,46]. Similarly, recent high-temperature fretting studies have reported that tribolayers formed by compaction and tribo-sintering of wear debris can significantly affect friction fluctuations and wear rate at temperatures such as 550 °C and 750 °C [14]. Thus, 600 °C and 800 °C were chosen to compare two distinct regimes: a lower high-temperature condition where retained oxide-rich debris may stabilize the contact, and a higher temperature condition where the same third-body process may become unstable due to increased debris generation, coating damage, and material transfer. It should be noted that additional intermediate temperatures would be required to precisely define the transition boundary between these regimes which will be incorporated in the future studies.

In the present study, each fretting condition was repeated twice using the available coated specimens. For each temperature condition, both repeat tests were performed on the same coated sample at separate wear locations while maintaining the target temperature throughout the test sequence. This approach was used to avoid repeated thermal cycling of the coating, which could alter the microstructure, residual stress state, and damage response prior to subsequent testing. Therefore, the results are interpreted as a comparative assessment of the temperature-dependent fretting response, while additional repetitions would be required for broader statistical validation and would be incorporated in the future studies.

A confocal microscope was used to evaluate the wear depth at the conclusion of the test, and the coefficient of friction was continually recorded. The CoF was recorded for each temperature condition. The average CoF was calculated by averaging two trials to ensure reliability. Confocal laser microscopy (Olympus LEXT 4000, Houston, USA) was used to assess the wear track and calculate wear depth. The wear depth profile was derived from the average of one horizontal and one vertical profile corresponding to the maximum depth as assessed by the wear scar. Origin software was used to graph the friction curve, specific wear rate and the wear depth profile. The wear volume was estimated from the confocal wear profile by integrating the cross-sectional wear area. The integrated area obtained from the profile perpendicular to the sliding direction was multiplied by the reciprocating wear track length to estimate the wear volume. The calculated volume was then normalized by the applied load and total sliding distance to obtain the specific wear rate. The wear tracks and counter balls from the post-sliding wear test were analyzed by scanning electron microscopy (SEM), and their chemical composition was assessed by energy-dispersive X-ray spectroscopy (EDS). The sub-surface analysis was performed by Focus Ion Beam Scanning (FIB) (FEI Helios 600 NanoLab 660, Thermo Fisher Scientific, USA). A thin layer of Ga/Pt was deposited on top to protect the surface.

3. Results

3.1. Coating characteristics

Fig. 1(a) shows a schematic of the HEO sample, which was produced using HVOF for the bond coat and SPS for the topcoat. Fig. 1(b) to (d) show the cross-sectional SEM images of SPS-sprayed HEO coatings. The coating exhibited a dense, homogeneous microstructure with minimal porosity and interspersed vertical cracks throughout the coating thickness, as evident from SEM image 1(b). The HEO topcoat thickness was measured to be approximately ~195 μm (See Fig. 1(c)). The vertical crack density was quantified as ~11 cracks/mm, and the porosity level was measured to be ~5% as reported by Vakilifard et al. [34]. Fig. 2 shows the EDS elemental mapping across the coating cross-section. This confirmed the presence of the constituent elements associated with the HEO $(Y_{0.2}Nd_{0.2}Gd_{0.2}Sm_{0.2}Dy_{0.2})_2Zr_2O_7$. The table in Fig. 2(d) represents the atomic percentage of each element present in the HEO Topcoat. The elemental distribution reported in the table confirms a uniform distribution of the rare-earth species and Zr within the topcoat. No pronounced elemental segregation was evident within the analyzed region.

The Vickers hardness of the HEO coating was 465 ± 21 HV, measured on the topcoat using 10 valid indents. This value represents the apparent hardness of the SPS-sprayed coating rather than the intrinsic hardness of a fully dense bulk HEO ceramic. Therefore, it should be interpreted considering the coating microstructure, including inter-splat boundaries, residual porosity, and vertical/branching cracks, which can reduce the measured indentation hardness even when pores and cracks are avoided during indentation.

The crystal structures of the synthesized HEO powder and the as-sprayed coating were examined by XRD, shown in Fig. 3. The synthesized powder exhibited a pyrochlore-type ordered structure. Since pyrochlore is an ordered derivative of the fluorite structure, its main diffraction peaks overlap with fluorite-related fundamental reflections, while the weak superstructure reflections are used to identify long-range pyrochlore ordering. In the present powder, weak but identifiable pyrochlore superstructure reflections, including the (115), (133), and (135) peaks, were observed. These reflections confirm the presence of pyrochlore-type ordering in the powder. Rietveld refinement of the powder XRD pattern gave a refined lattice parameter of 10.52 Å with a weighted profile R-factor, Rw, of approximately 15%. This level of agreement is acceptable for complex multicomponent oxides and supports that the weak superstructure reflections are associated with pyrochlore-type ordering. The refined lattice parameter is also close to the value reported by Hutterer et al. for a similar high-entropy zirconate composition [47]. After SPS deposition, these weak pyrochlore superstructure reflections were no longer detected in the coating, indicating a reduction or loss of long-range pyrochlore ordering during spraying. No additional secondary phases were detected within the resolution of XRD.

Hardness was used as an initial indicator of the coating's mechanical response. However, additional characterization would be required for a more complete mechanical correlation. Elastic modulus, fracture toughness, and adhesion strength should also be evaluated, and it would be incorporated in future studies. Therefore, in the present work, the wear mechanisms were primarily interpreted from direct experimental observations. To supplement the discussion, friction evolution, wear depth and specific wear rate, debris morphology, SEM/EDS analysis,

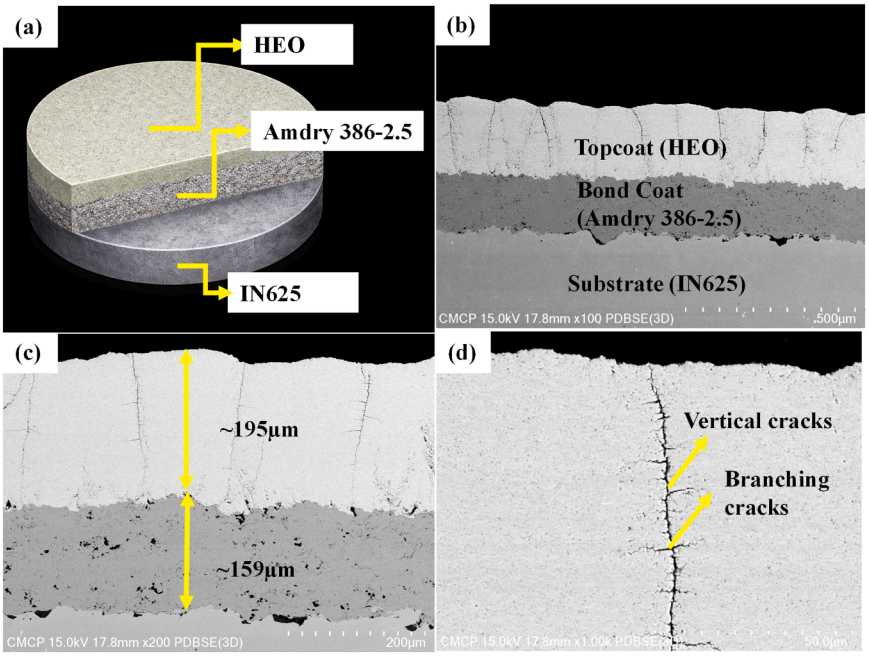

Fig. 1. (a) Schematic representation of the sample as sprayed. (b-d) Cross-sectional SEM images of SPS-sprayed HEO coatings at different magnifications.

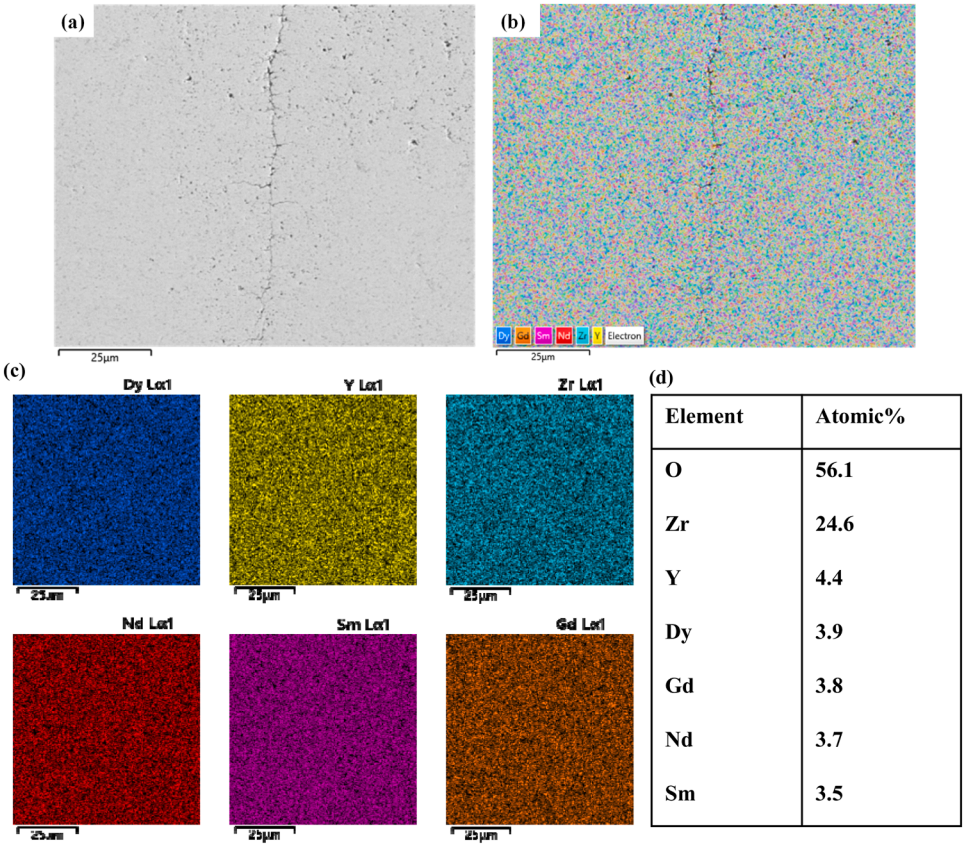

(d)

Element	Atomic%
O	56.1
Zr	24.6
Y	4.4
Dy	3.9
Gd	3.8
Nd	3.7
Sm	3.5

Fig. 2. (a) Backscattered image of the HEO coating cross section, (b) layered elemental distribution, (c) EDS maps, and (d) Tabulated chemical composition of the studied area in the coating, with the atomic percentage of elements.

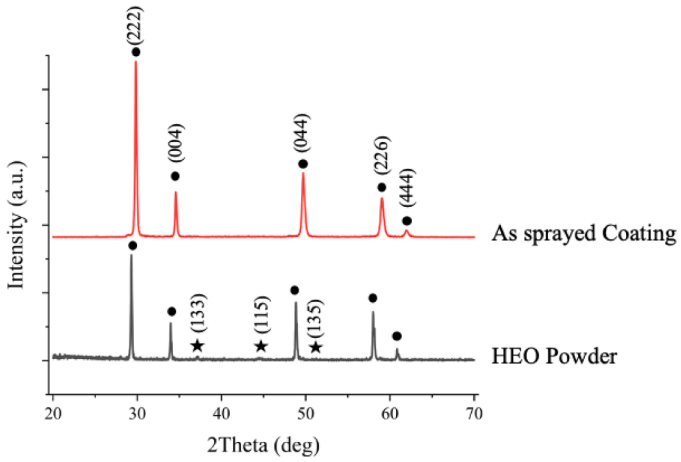

Fig. 3. XRD patterns of the synthesized HEO powder and the as-sprayed SPS HEO coating.

and coating damage were considered.

3.2. Fretting wear behavior

Fig. 4 presents the coefficient of friction (CoF) as a function of time, averaged over two trials, for SPS-sprayed HEO coatings tested against a SiC ball under a 15 N normal load at 600 °C and 800 °C. The coating tested at 800 °C shows noticeably higher friction, nearly twice that at 600 °C, particularly during the running-in stage. At 600 °C, the running-in phase extends to roughly the first 500 s. During this period, the CoF typically lies in the ~0.15–0.20 range, with an initial spike at the start and another spike near the end of the running-in interval. After this break-in, the friction transitions smoothly into a steady-state regime and stabilizes at approximately 0.09–0.10, remaining consistent for the rest of the test. In contrast, at 800 °C, the running-in period lasts longer, up to about 1000 s, with CoF values averaging around ~0.27–0.30. Beyond the first 1000 s, the friction begins to decrease and gradually stabilizes by ~2000 s, settling at an average CoF of ~0.25. Compared to 600 °C, the 800 °C curve shows more pronounced fluctuations before reaching steady state. Despite differences in running-in behavior and steady-state levels, the average CoF value remains below ~0.3 for both temperatures.

Fig. 5 illustrates the wear depth profiles of the SPS-sprayed HEO coatings evaluated at 600 °C and 800 °C. The wear profile plotted here is the average of the maximum wear depth along the horizontal and vertical profiles. The findings suggest that the wear depth under 800 °C testing conditions is significantly greater than that under 600 °C conditions. The wear depth at 800 °C is around 43 ± 2 μm, which is significantly higher than the wear depth at 600 °C (7 ± 2 μm). Corresponding to the wear depth profiles the specific wear rate calculated at 600 °C is ~$3 \pm 2 \times 10^{-7}$ mm³ /N·m and for 800 °C its ~$2.6 \pm 0.6 \times 10^{-6}$ mm³ /N·m. The fluctuations in the wear profile at 800 °C are a result of microchips and brittle fracture, which generate the peaks and valleys, as discussed in the subsequent sections.

3.3. Comparison with reported high-temperature tribological studies

To qualitatively compare the present fretting results, in Table 4 we have compared the coefficient of friction and wear behaviour of the present defective-fluorite HEO coating with previously reported selected high-temperature tribological coatings. The table reported HEO/high-entropy ceramic systems, MoS_2-based adaptive coatings, and oxide-based lubricious coatings. It should be noted that the comparison should not be interpreted as a direct ranking because the reported studies differed in contact geometry, counterface material, load, sliding mode, and test environment.

The Table 4 compares the present fretting response with the published high-temperature tribological coatings and oxide based lubricious systems. The comparison is intended to provide a contextual benchmark rather than a direct ranking as the reported studies differ in testing conditions (such as contact geometry, counterface material, siding mode and testing environment etc). Nevertheless, the comparison shows that the present HEO coating exhibits a competitive low-friction response at 600 °C, with a CoF of ~0.1 and a wear depth of ~7 μm with wear rate of ~3×10^{-7} mm³ /N·m. This is comparable to the recent oxide assisted lubricious system. However, the response at 800 °C highlights an important limitation and that is, despite a moderate CoF of ~0.25, the wear depth (consequently wear rate) increased substantially (wear depth increased to ~43 μm and wear rate to ~2.6×10^{-6} mm³/N·m). Along with this, there was a significant transfer of coating to the counterface which will be discussed in the subsequent sections.

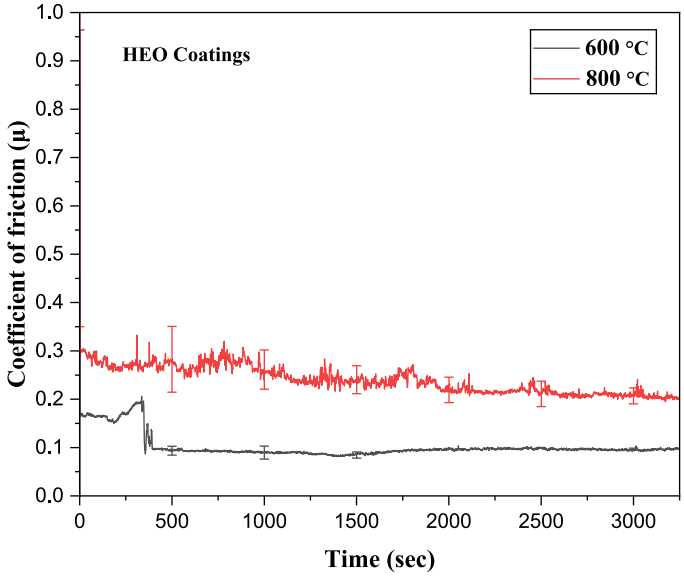

Fig. 4. Coefficient of friction (CoF) versus sliding time (sec) for SPS-sprayed HEO coatings tested at 600 °C and 800 °C.

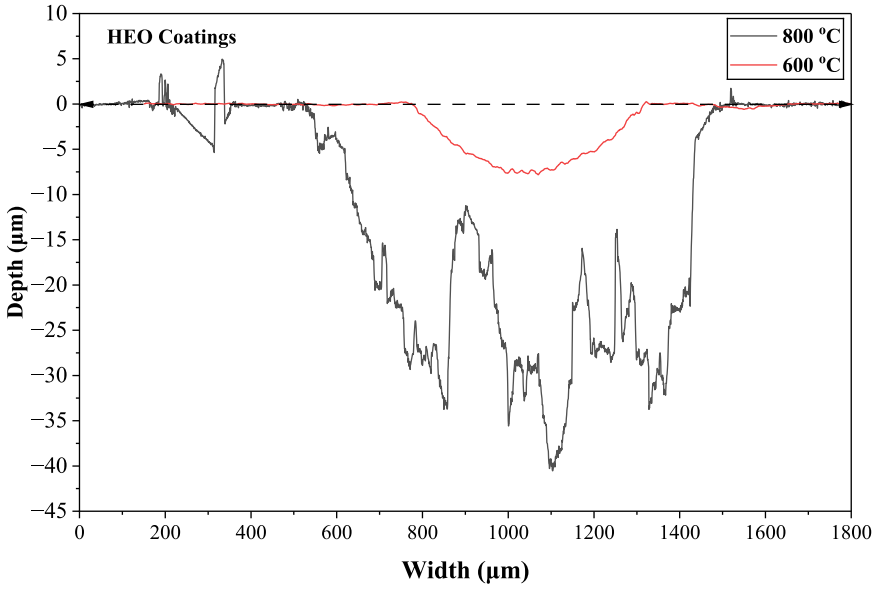

Fig. 5. Maximum Wear depth profile of SPS-sprayed HEO coatings at 600 °C and 800 °C.

Table 4
Comparison of present HEO fretting response with recent high-temperature tribological coating/lubricious systems.

Coating/material system	Test condition	Temperature	CoF	Wear metric
HEO coating (present study)	Fretting against SiC, 15 N, 300 µm stroke, 60 Hz	600 °C	~0.10	~3×10^{-7} mm³ /N·m
HEO coating (present study)	Fretting against SiC, 15 N, 300 µm stroke, 60 Hz	800 °C	~0.25	~2.6×10^{-6} mm³ /N·m
Mo_2N/MoS_2/Ag adaptive coating [48]	Sliding against Si_3N_4 in air	600 °C	~0.10 for optimized coatings	~8×10^{-6} to 1×10^{-5} mm³ /N·m
PS304 self-lubricating coating [49]	Thrust-washer tests against Rene 41/Inconel X−750	538 °C	~0.4	1.5–3 × 10^{-4} mm³ /N·m
NiCoCrAlYTa/Ag/Mo composite coating [50]	Sliding against Al_2O_3	800 °C	~0.22	1.1 × 10^{-5} mm³ /N·m
Spinel-oxide-enabled self-lubricating Inconel surface [51]	High-temperature tribological testing	600 °C−900 °C	0.10–0.32	Not directly comparable
SPS CuO coating [52]	Dry sliding	300 °C	~0.46	32 × 10^{-5} mm3/N.m
SPS Ta_2O_5 coating [53]	Dry sliding	300 °C	~0.8	54 × 10^{-5} mm³ /N·m
Carbon-deficient high-entropy carbide ceramic [54]	High-temperature sliding in vacuum	900 °C	0.31 ± 0.01	< 10^{-6} mm³ /N·m
High-entropy sublattice nitride coating, (Al,Cr,Nb,Ta,Ti)N [37]	Dry ball-on-disk against Al_2O_3	700 °C	CoF dropped from ~0.9 to ~0.3 after ~10 m sliding	Wear track nearly indistinguishable at 700 °C
High-entropy sublattice oxide coating, (Al,Cr,Nb,Ta,Ti)O_2 [37]	Dry ball-on-disk against Al_2O_3	20 °C−700 °C	Not valid; coating failed prematurely	Not comparable
APS NiCrAlY-MoO_3/CoO composite coating [55]	High-temperature sliding	800 °C	0.30	8.32 × 10^{-6} mm³ /N·m
MoS_2-TiO_2-Ag composite [56]	High-temperature sliding	450 °C	~0.26	1.2 × 10^{-5} mm³ /N·m
Plasma-sprayed NiCr-Cr_3C_2-BaF_2/CaF_2 coating [57]	High-temperature sliding	Up to 800 °C	CoF decreased with increasing temperature	Wear rate decreased from 600 to 800 °C, but oxidation exposure reduced wear resistance

3.4. Ex-situ analysis of wear track and counterface

The top-down SEM images of the wear tracks as well as EDS maps have been presented in Fig. 6 For 600 °C (See Fig. 6(a)& 6(b)), from the image, the wear track was extremely minor and hard to notice. It remained largely intact and appeared to be covered by a powder-like oxide layer, uniformly distributed across the scar. This appearance is consistent with the formation of a stable third-body layer. Notably, despite the presence of pre-existing columnar cracks in the as-deposited coating (See Fig. 1(b, c, & d)), no evidence of secondary cracking or chipping was detected within the 600 °C wear track. This suggests that the coating likely retained sufficient hardness and maintained low adhesion at this temperature. Hence, minimizing the material transfer to the counterface. It could also be inferred that the loose oxide debris may have infiltrated and cushioned the columnar gaps, consequently minimizing the CoF and supporting low wear depth.

At 800 °C, the coating maintained an average value of ~0.25 as its CoF, as discussed in previous sections, but the wear track morphology changed significantly. The SEM images (See Fig. 6(c)& 6(d)) illustrate that the wear track morphology became significantly more damaged, with the presence of microcracks, pits, chipping, and a substantial amount of loose debris. The corresponding increase in wear depth to ~43 µm (See Fig. 5) at this temperature suggests that the coating became less mechanically stable under repeated thermo-cyclic shear.

To further elucidate the wear mechanism, the SiC counterfaces were analyzed via SEM and EDS mapping (Fig. 7&8). At 600 °C, the SiC surface remained relatively clean, with SEM observations revealing only a sparse distribution of fine, loose particulates. From the EDS mapping, it was confirmed that these are oxide fragments, primarily showing signals for O and Zr, which correlated to the HEO coating composition

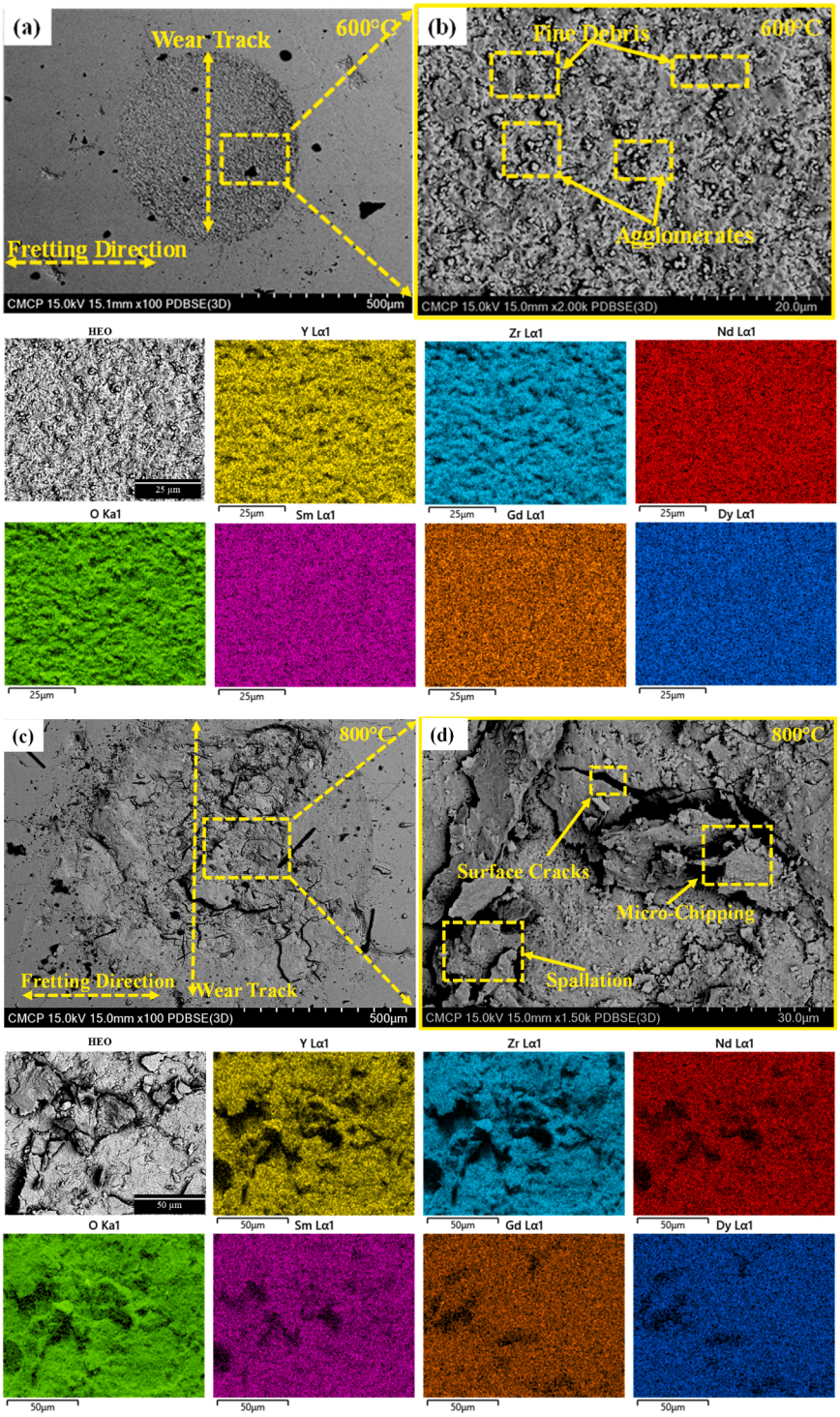

Fig. 6. SEM images and EDS mapping of the wear track for SPS-sprayed HEO coatings: (a, b) 600 °C (c, d) 800 °C.

(see Fig. 7(a) & 7(b)). There was no evidence observed of continuous or smeared transfer film on the counterface at 600 °C. Hence, it could be inferred that there was no significant adhesion between the counterface and the coating. On the other hand, the counterface morphology at 800 °C underwent an interesting shift, exhibiting a dense accumulation of both powdered debris and sticky transfer patches. The EDS analysis in these regions also revealed the expected presence of HEO elements, which could be attributed to the localized spallation of significant coating segments, which then consequently adhered to and smeared across the SiC counterface (see Fig. 8(a) & 8(b)). The effective contact between the counterface and the wear track also increased at 800 °C. This transition from the third body rolling mechanism at 600 °C to a more pronounced adhesive-transfer regime at 800 °C could explain the almost five-fold increase in wear depth and the higher frictional resistance. Not only that, the intermittent spikes as are observed in the friction curve for 800 °C (see Fig. 3) could be likely due to this phenomenon.

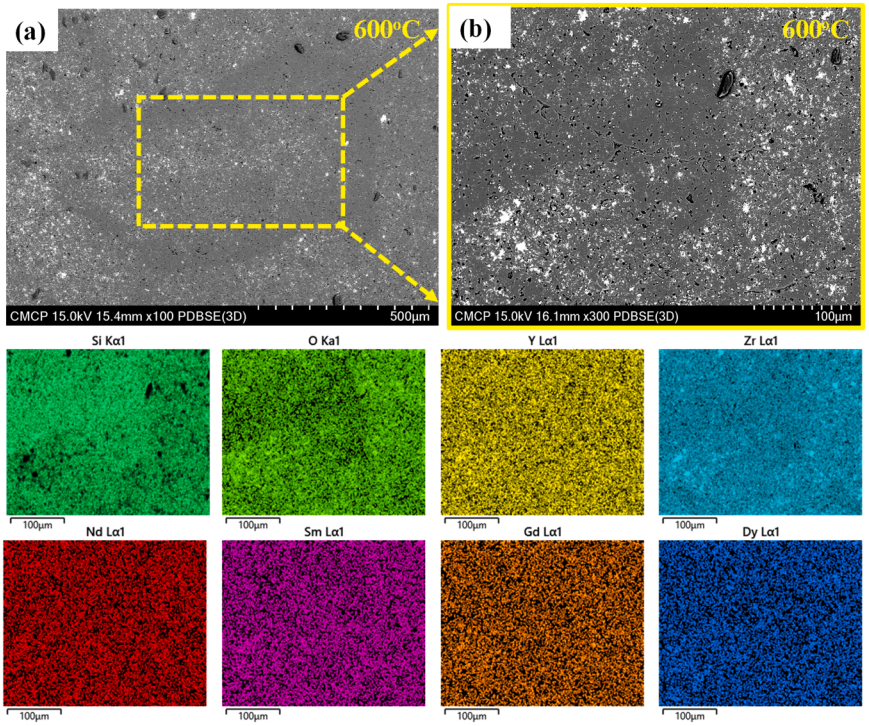

Fig. 7. SEM images and EDS maps of the counterface for SPS- sprayed HEO coatings at 600 °C (a & b).

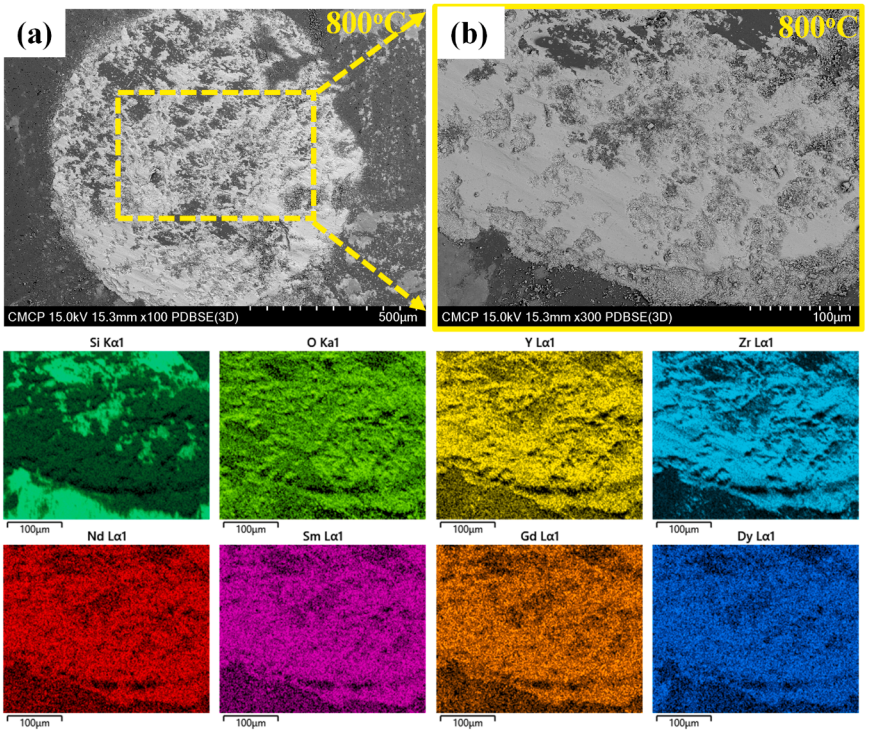

Fig. 8. SEM images and EDS maps of the counterface for SPS- sprayed HEO coatings at 800 °C (a & b).

3.5. Sub-surface analysis of wear track

The subsurface material properties and microstructure beneath the wear track are generally altered during sliding under demanding conditions due to stress transfer and contact loading, which influence friction and wear mechanisms. To evaluate these effects, FIB/SEM analysis was conducted on both the worn regions (within the wear track) and adjacent unworn regions for tests performed at 600 °C and 800 °C. At 600 °C (see Fig. 9(a)), the unworn subsurface showed pre-existing pores along with vertically oriented cracks and occasional near-surface microcracks. It is likely that during fretting, due to the higher contact stresses between the coating and counterface in the running-in stage, the interconnection and coalescence of smaller pores and vertical cracks, accompanied by asperity pull-out during sliding, contributed to the

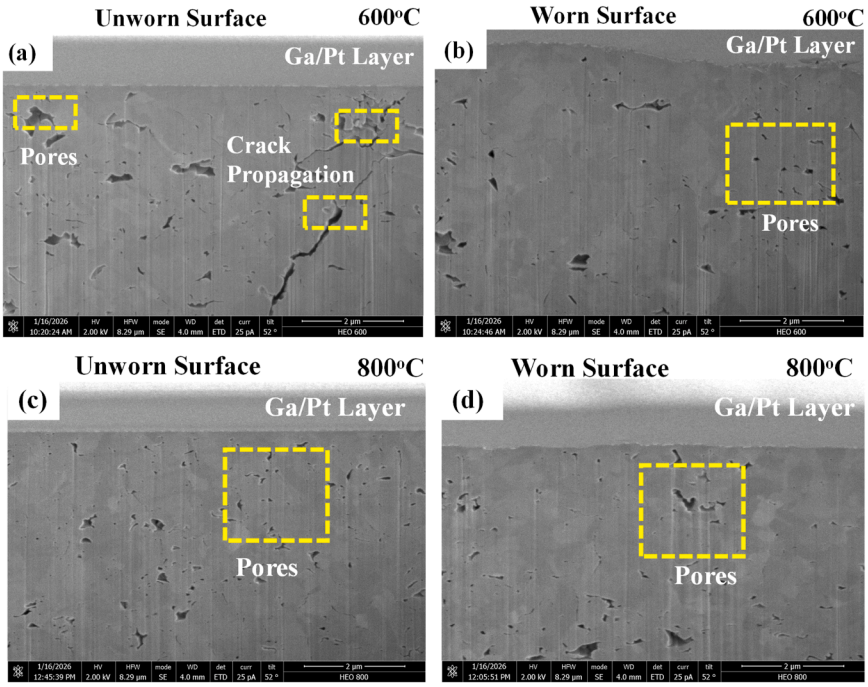

Fig. 9. FIB/SEM images for SPS- sprayed HEO coatings at 600 °C (a&b); and 800 °C (c&d).

formation of wear debris. This debris likely rolled between the contacting surfaces, reducing direct contact between the coating and the counterface, as confirmed by counterface analysis, and resulted in relatively low material removal after the initial sliding cycles. Importantly, no microcracks or significant defects were observed beneath the wear scar (see Fig. 9(b)), indicating that the coating subsurface remained largely intact and provided effective resistance to deformation under high contact stresses. In contrast, at 800 °C (see Fig. 9(c) & 9(d)), both the worn and unworn subsurface were characterized by a higher density of pores, and more frequent pore linking was evident. Under continued thermo-mechanical shearing, such a pore-dense microstructure provides multiple sites for crack initiation and facilitates crack linking and material pull-out, promoting progressive material removal, as observed in the higher wear depth (see Fig. 5) at this temperature. As was also evident from the SEM analysis of Counterface (see Fig. 8) and wear scar (see Fig. 6(c) & 6(d)), the brittle fracture, microchipping, and subsequent damage on the contact region could be attributed to the pore-dense microstructure.

4. Discussion

4.1. Coating characteristics

The cross-sectional SEM observations (see Fig. 1(b, c, & d)) revealed that SPS-sprayed HEO coatings deposited on an Amdry 386–2.5 bond coat exhibited a dense and relatively uniform microstructure with interspersed vertical cracks throughout the coating. Branching cracks were also observed within the coating (see Fig. 1(d)). This dense segmented microstructure could be attributed to the high-energy axial SPS deposition conditions, as discussed by Vakilifard et al. [34]. In SPS, the in-flight particle temperature and impact velocity strongly influence particle melting, splat flattening, inter-splat bonding, and overall coating build-up, as has been extensively discussed in the work done elsewhere [34,58,59]. The relatively high plasma enthalpy of 10.6 kJ/L, together with the measured in-flight particle temperature of 3404 ± 142 °C and particle velocity of 592 ± 24 m/s, suggests that a large fraction of the fine HEO particles was sufficiently molten before impact. This promoted effective splat flattening and bonding, resulting in the dense microstructure and low porosity observed in the as-sprayed coating.

Similar behaviour was reported in our previous work on SPS high-entropy zirconate coatings, where higher plasma enthalpy and higher particle temperature and velocity promoted denser vertically cracked microstructures, while lower-energy conditions favored more porous columnar microstructures [34]. In the present coating, the vertical crack density was approximately 11 cracks/mm, with cracks mainly oriented through the coating thickness and with some branching features. The formation of this crack network is likely related to the dense coating build-up and the accumulation of residual stresses during deposition and cooling.

The measured hardness is lower than values often reported for dense pyrochlore-structured high-entropy oxide ceramics. This difference is expected because the present value was obtained from an SPS-sprayed coating, not a fully dense sintered bulk material. Plasma-sprayed ceramic coatings typically contain microstructural features such as porosity, interlamellar pores, incomplete inter-splat bonding, and thermal stress-relief cracks formed during the rapid solidification of splats. These features can lower the measured coating hardness compared with that of dense bulk ceramics [60]. Moreover, the XRD results showed that the as-sprayed coating exhibited a fluorite-type structure after SPS deposition, while the starting powder was pyrochlore. Therefore, the reported hardness should be regarded as the effective hardness of the as-sprayed fluorite-type HEO coating, rather than the intrinsic hardness of a dense pyrochlore HEO ceramic.

4.2. Fretting wear behaviour and worn surface morphology

Fretting is high-frequency, small-displacement oscillatory sliding that occurs at the interface between two contacting solid surfaces. Because the motion is repetitive and confined to a very short stroke, the resulting damage is typically multifactorial, with contributions from adhesive junction formation and rupture, debris-driven abrasion, tribochemical/oxidative reactions, and cyclic fatigue-related cracking or delamination [61]. Under normal loading, intimate asperity contact can facilitate the formation of adhesive junctions. During oscillatory motion, these junctions are repeatedly sheared, which can initiate surface cracking and generate wear debris. Because fretting involves very small

displacement amplitudes, the generated debris is often retained within the contact, where it can participate in tribochemical reactions (e.g., oxidation) and influence subsequent wear [62].

In this study, the fretting experiments were performed at 600 °C and 800 °C, and the average CoF remained below 0.3 at both temperatures. However, the friction response was clearly temperature dependent, with lower and more stable friction at 600 °C than at 800 °C. At 600 °C, the running-in period lasted approximately 500 s. During this stage, friction was likely controlled by direct asperity interactions, removal of surface contaminants, and the initial formation of wear debris. The comparatively smooth initial surface, with roughness below 1 μm, may also have contributed to the early low-friction response before the contact evolved under repeated sliding [53,63]. During the initial running-in period, surface contaminants were likely removed from the contact, which increased direct adhesion between the SiC counterface and the coating. This contributed to the gradual increase in friction observed toward the end of the running-in stage [64]. Interestingly, during fretting at 600 °C, a pronounced decrease in CoF was observed at approximately 500 s, followed by a stable low-friction regime. As fretting progressed, debris generated by local asperity removal and limited material pull-out was retained within the contact. With continued sliding, this retained debris likely formed a more continuous third-body layer between the counterface and the coating. As a result, direct interaction between the SiC counterface and the coating was reduced, and shear was increasingly accommodated within the interfacial debris layer. This transition explains the sudden decrease in CoF after the running-in stage and the subsequent stable friction response. This interpretation is consistent with third-body concepts of friction and with fretting studies that associate CoF reduction with a transition from two-body contact to three-body accommodation, and in some cases, with the formation of protective oxide or glaze-like layers [65-69].

This interpretation is also supported by the worn-surface morphology (see Fig. 6(a) & 6(b)) and sub-surface observations reported in Fig. 9(a) & 9(b). The wear scar in Figs. 6(a) and 6(b) is covered by a loose powder like debris layer. No clear secondary cracking, chipping or severe fracture features were observed. This suggests that the debris layer helped in reducing the direct contact stresses and limited material removal. The subsurface observations (see Fig. 9(a) & 9(b)) support this mechanism. From the images it could be observed that region beneath the wear scar remained largely intact after testing at 600 °C, indicating that the damage did not propagate deeply into the coating.

It's important to note that the as-deposited coating contained interspersed vertical cracks (See Fig. 1(b,to d)). At 600 °C, these pre-existing crack features did not appear to evolve into visible chipping within the wear track. Therefore, under this relatively milder condition compared to 800 °C, these cracks likely acted mainly as strain-accommodation features rather than active damage paths. Vertically segmented microstructures are widely recognized for improving strain tolerance in thermal-sprayed ceramic topcoats [34,70]. In the present case, these cracks may also have provided local sites for debris retention, supporting third-body stabilization and contributing to shallow wear and stable friction.

On the other hand, at 800 °C, the CoF showed a longer, more dynamic running-in response than at 600 °C. The curve exhibited a higher initial friction level, followed by fluctuations before reaching a more stable regime at approximately 0.25. This behaviour suggests that a third-body layer also formed at 800 °C, but it was repeatedly disrupted before becoming sufficiently stable, as discussed elsewhere [69,71,72]. The initial decrease in friction could be attributed to the initial surface conditioning [53,63] and the onset of third body accommodation. While the subsequent intermittent spikes likely reflect repeated breakdown, displacement, and reformation of the debris layer. In fretting contacts, such repeated formation and destruction of debris beds during running-in has been widely reported [67,69,72]. Beyond the initial running-in period, the gradual decrease in CoF can be attributed to progressive compaction and partial stabilization of oxide debris within the contact. At elevated temperature, retained oxide debris can become more compacted under repeated shear, allowing part of the sliding to be accommodated within the tribolayer and reducing friction [73-75].

These observations could be correlated with the SEM images for the worn surfaces (see Fig. 6(c) & 6(d)). Although the CoF at 800 °C remained below approximately 0.3, the wear damage was substantially more severe than at 600 °C. As is evident from the SEM images, the wear track underwent substantial disruptions marked by micro chipping, crack formation, and abundant loose debris. The SEM images and EDS mapping for the counterface (see Fig. 7) also showed adhesive transfer patches and accumulated debris containing HEO-related elements. These observations indicate that the contact at 800 °C involved stronger adhesive interactions and less stable third-body protection than at 600 °C. Under these conditions, the localized fracture and pull-out could intermittently expose fresh coating material and introduce larger fragments into the contact, producing short-lived CoF spikes superimposed on the overall friction trend [72-74]. In addition, the subsurface FIB images at 800 °C (see Fig. 9(c) & 9(d)) showed a pore-dense microstructure in both worn and unworn regions. Pore coalescence under cyclic thermo-mechanical shear provides crack initiation sites and promotes fragment detachment, which is consistent with chipping and the higher wear depth at this temperature. Under this more severe condition, two factors are therefore inferred to be more influential (i) Stronger adhesive interaction, which increases the real contact area and promotes larger junctions, and (ii) interaction of cyclic shear with the pre-existing vertical cracks, which can act as preferential paths for inter-columnar cracking, local delamination, and material pull-out at higher severity. A schematic of the operating wear mechanism for the SPS-sprayed HEO samples is shown in Fig. 10.

The different wear responses at 600 °C and 800 °C can be understood as a balance between third-body stabilization and coating damage accumulation. At 600 °C, frictional energy was likely dissipated mainly through shear within the retained third-body debris layer. This stabilized debris layer reduced direct interaction between the SiC counterface and the coating, thereby limiting material removal and supporting the low-wear response. At 800 °C, debris was still generated and may have helped maintain a relatively low CoF. However, the tribolayer was less stable, and the coating underwent more extensive crack linking, localized pull-out, and adhesive transfer. As a result, a larger fraction of the frictional energy was likely dissipated through damage-related processes rather than through stable interfacial shear. Under this more severe condition, the pre-existing vertical cracks and pores may have played a dual role. While they can improve strain tolerance and assist debris retention, they may also act as stress concentrators and preferential paths for cracking and material removal when the contact becomes more aggressive.

The possible contribution of coating chemistry should also be considered. EDS mapping of the counterface after testing at 800 °C showed HEO-related elements within the transferred debris, Fig. 8. This suggests that the interfacial third body was chemically complex and originated, at least partly, from the HEO coating. Such multi-cation oxide debris may contribute to shear accommodation once a compacted tribolayer is formed. However, the present study does not isolate the specific role of each cation, Y, Nd, Gd, Sm, and Dy. Therefore, the low-friction response is interpreted here in terms of the collective behaviour of the HEO chemistry and the debris-mediated third-body layer, rather than assigning individual lubricating roles to specific elements. Future studies using simplified reference oxides or systematically varied HEO compositions are needed to clarify the contribution of each constituent element to tribolayer formation, shear accommodation, and wear resistance.

Since the as-sprayed coating exhibited a fluorite-type structure before fretting, the difference in wear response between 600 °C and 800 °C is not attributed here to a pyrochlore-to-fluorite transformation during testing. Instead, the transition from stable third-body-mediated

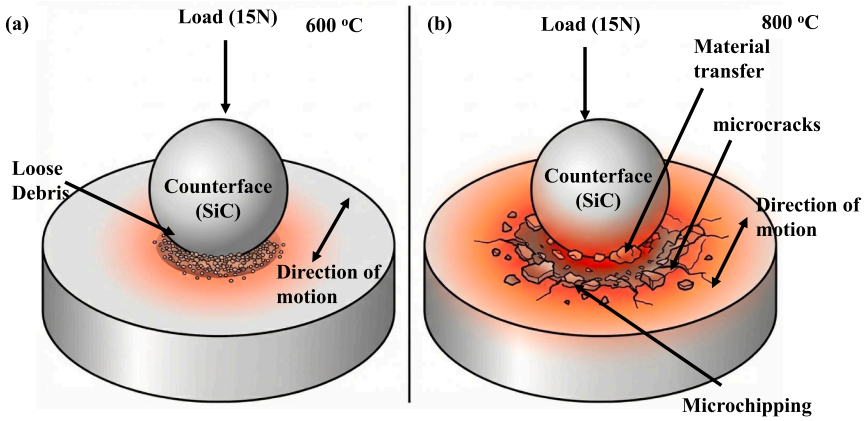

Fig. 10. Schematic of operating wear mechanisms of SPS sprayed HEO sample tested at (a) 600 °C, and (b) 800 °C.

wear at 600 °C to more severe adhesive transfer, crack linking, and pull-out at 800 °C is mainly associated with the temperature-dependent stability of the debris/tribolayer and the mechanical response of the dense vertically cracked coating. Nevertheless, localized tribo-induced structural changes inside the wear track cannot be fully excluded based only on the present XRD result. Post-wear micro-XRD or TEM analysis would be useful to confirm the local phase state after fretting and would be incorporated into future studies.

The thermal stability of the HEO coating within the fretting temperature range was also assessed by DSC. The DSC curve measured up to 800 °C, Fig. 11, did not show a pronounced thermal event associated with major phase decomposition or phase transformation. This supports the interpretation that the HEO coating remained thermally stable within the tested temperature range. However, DSC represents the bulk thermal response and does not directly confirm the local phase state inside the wear track after fretting. Therefore, post-test phase analysis of the worn region would still be required to fully determine whether localized tribo-induced structural changes occurred during sliding and would be a part of future studies.

Overall, this work highlights the potential of SPS- sprayed HEO coatings as protective, low-friction surfaces for high-temperature tribological applications. To strengthen their wear resistance further, future studies should focus on tailoring composition and processing to achieve a better hardness-toughness balance, including exploring the incorporation of additives (e.g., Ag and Co) that have been reported to improve mechanical response and tribological performances. Additional work is also needed to evaluate long-duration reliability and stability under more severe working conditions. Additionally, further studies on the effect of varying coating deposition parameters for the SPS process, which may influence the coating microstructures, and subsequently testing them under service-related conditions, could provide deeper insights into the working of these HEO-based coatings.

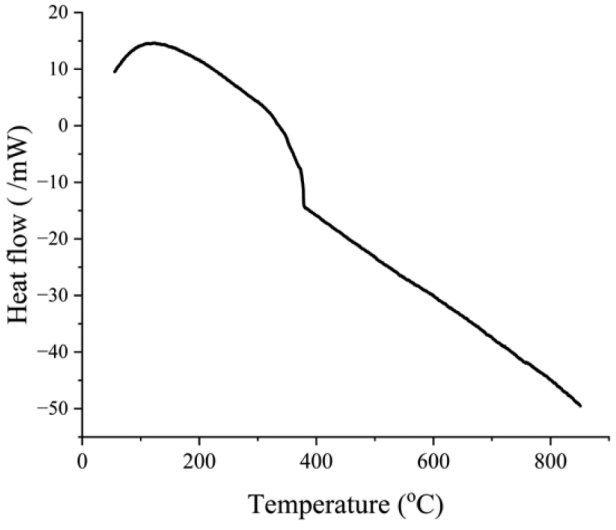

Fig. 11. DSC heat flow curve of the SPS-sprayed HEO coating measured from room temperature to 800 °C.

5. Conclusion

In this study $(Y_{0.2}Nd_{0.2}Gd_{0.2}Sm_{0.2}Dy_{0.2})_2Zr_2O_7$ high-entropy oxide (HEO) coatings were deposited by suspension plasma spraying (SPS) and evaluated under high-temperature fretting conditions at 600 °C and 800 °C. The as-deposited coatings exhibited a dense and relatively uniform microstructure with interspersed vertical cracks and a room-temperature hardness of 465 ± 21 HV. The coatings showed moderately low-friction behaviour at both temperatures, with steady-state CoF values remaining below approximately 0.3. However, the wear response and damage severity were strongly temperature dependent.

At 600 °C, the coating showed better overall tribological performance, with a limited wear depth of 7 ± 2 μm and a wear rate of approximately 3×10^{-7} mm³ /N·m. This response was associated with the formation and retention of fine oxide-rich third-body debris within the fretting contact. The retained debris likely helped accommodate shear, reduce direct interaction between the SiC counterface and the coating, and maintain stable low friction. The vertical and branching cracks may have also contributed by improving strain tolerance and providing local sites for debris retention, thereby supporting shallow wear.

At 800 °C, the wear depth increased significantly to 43 ± 2 μm, with a wear rate of approximately 2.6×10^{-6} mm³ /N·m. The worn surface showed micro-cracking, pull-out, localized spalling, and coating transfer to the counterface. Under this more severe condition, the crack and pore network likely acted as stress concentration sites, promoting crack linking and localized material removal. In addition, the higher temperature may have enhanced adhesive interactions between the SiC counterface and the coating while reducing the stability of debris accommodation within the contact. As a result, the dominant wear mechanism shifted from stable third-body accommodation at 600 °C to adhesion- and fracture-assisted material removal at 800 °C.

Overall, this study highlights the potential of SPS-deposited HEO coatings as protective surfaces for high-temperature fretting applications, particularly where stable third-body debris formation can be maintained. However, the increased wear at 800 °C shows that low friction alone is not sufficient to ensure coating durability under more severe thermal and mechanical conditions. Future work should focus on longer-duration fretting tests, intermediate-temperature studies, additional repeat testing for broader statistical validation, and high-

temperature mechanical characterization, including hardness, elastic modulus, and fracture toughness. Detailed tribolayer chemistry and transfer-film analysis would also help clarify the interfacial mechanisms controlling the transition from stable low-friction behaviour to damage-dominated wear.

CRediT authorship contribution statement

Payank Patel: Writing – review & editing, Software, Methodology, Investigation, Formal analysis, Data curation. **Ikshita Chaturvedi:** Writing – original draft, Visualization, Software, Methodology, Investigation, Formal analysis, Data curation. **Pantcho Stoyanov:** Writing – review & editing, Supervision, Resources, Project administration, Funding acquisition, Conceptualization. **Martin Dienwiebel:** Writing – review & editing, Methodology, Data curation. **Christian Moreau:** Writing – review & editing, Resources, Project administration, Funding acquisition, Conceptualization. **Hamideh Vakilifard:** Writing – review & editing, Methodology, Data curation. **Fadhel Ben Ettouil:** Writing – review & editing, Methodology, Data curation.

Declaration of Competing Interest

The authors declare that they have no known competing financial interests or personal relationships that could have appeared to influence the work reported in this paper.

Acknowledgements

The authors gratefully acknowledge financial support from the Natural Sciences and Engineering Research Council of Canada (NSERC) Discovery grant. We also thank the National Research Council Canada (NRC) and the members of the Surftec Industrial R&D Group for their support throughout this investigation and publication. In addition, the authors acknowledge funding from the Consortium de recherche et d'innovation en transformation métallique (CRITM) through its Support Program for Research and Innovation Organizations (PSO) and recognize Concordia University as NRC's academic collaborator on this project. The authors would also like to extend their gratitude to Dr. Dmytro Kevorkov from the Facility for Electron Microscopy Research at Concordia University for his assistance with advanced characterization.

References

[1] P. Stoyanov, K.M. Harrington, A. Frye, Insights into the Tribological Characteristic of Cu-Based Coatings Under Extreme Contact Conditions, JOM 72 (6) (2020) 2191–2197, https://doi.org/10.1007/s11837-020-04087-7.
[2] F.S. Pettit, G.H. Meier, Oxidation and Hot Corrosion of Superalloys, in: M. Gell, C. S. Kortovich, R.H. Bricknell, W.B. Kent, J.F. Radavich (Eds.), Superalloys 1984: Proceedings of the Fifth International Symposium on Superalloys, Warrendale, PA, USA: The Metallurgical Society of AIME, 1984, pp. 651–687, https://doi.org/10.7449/1984/Superalloys_1984_651_687.
[3] P. Patel, et al., Dry sliding wear and subsurface deformation mechanisms of inconel 718 at room and elevated temperatures, J. Mater. Sci. 61 (13) (2026) 9015–9030, https://doi.org/10.1007/s10853-026-12365-z.
[4] P. Patel, et al., Dry sliding friction and wear behavior of HVOF sprayed FeCrMnCoNi high entropy coatings (HECs) at room and elevated temperatures, Surf. Coat. Technol. 507 (2025) 132138, https://doi.org/10.1016/j.surfcoat.2025.132138.
[5] P. Patel, et al., Influence of aluminum addition on the microstructure and tribomechanical behavior of HVOF-sprayed AlxFeCrMnCoNi high entropy coatings (HECs), J. Alloy. Compd. 1039 (2025) 182854, https://doi.org/10.1016/j.jallcom.2025.182854.
[6] J.-W. Yeh, et al., Nanostructured High-Entropy Alloys with Multiple Principal Elements: Novel Alloy Design Concepts and Outcomes, Adv. Eng. Mater. 6 (5) (May 2004) 299–303, https://doi.org/10.1002/adem.200300567.
[7] C. Oses, C. Toher, S. Curtarolo, High-entropy ceramics, Nat. Res. (Apr. 01, 2020), https://doi.org/10.1038/s41578-019-0170-8.
[8] P. Patel, A. Roy, N. Sharifi, P. Stoyanov, R.R. Chromik, C. Moreau, Tribological Performance of High-Entropy Coatings (HECs): A Review, Materials 15 (10) (2022), https://doi.org/10.3390/ma15103699.
[9] T.Z. Ward, et al., High entropy ceramics for applications in extreme environments, Institute of Physics, Apr. 01, 2024, https://doi.org/10.1088/2515-7639/ad2ec5.
[10] J. Gild, et al., High-Entropy Metal Diborides: A New Class of High-Entropy Materials and a New Type of Ultrahigh Temperature Ceramics, Sci. Rep. 6 (1) (2016) 37946, https://doi.org/10.1038/srep37946.
[11] P. Sarker, et al., High-entropy high-hardness metal carbides discovered by entropy descriptors, Nat. Commun. 9 (1) (2018) 4980, https://doi.org/10.1038/s41467-018-07160-7.
[12] C.M. Rost, et al., Entropy-stabilized oxides, Nat. Commun. 6 (1) (2015) 8485, https://doi.org/10.1038/ncomms9485.
[13] B. Cantor, I.T.H. Chang, P. Knight, A.J.B. Vincent, Microstructural development in equiatomic multicomponent alloys, Materials Science Engineering A 375–377 (2004) 213–218, https://doi.org/10.1016/j.msea.2003.10.257.
[14] Y. Yang, H. Shang, H. Pei, J. Xu, Y. Liang, M. Pan, Role of temperature in tribolayers in fretting wear of γ-TiAl alloy, Friction 12 (5) (May 2024) 939–953, https://doi.org/10.1007/s40544-023-0807-x.
[15] C.H. Sathisha, Y. Arivu, S. Pramod, M.R. Sridhar, D. Kesavan, Exploring elevated temperature fretting wear behaviour of wrought and laser powder bed fusion IN718 superalloy, Tribol. Int. 192 (2024) 109279, https://doi.org/10.1016/j.triboint.2024.109279.
[16] M. Deng, et al., Comparative study on the fretting and sliding wear properties of micro-arc oxidation-treated aluminum alloy at different temperatures, Tribol. Int. 198 (2024) 109847, https://doi.org/10.1016/j.triboint.2024.109847.
[17] K. Luo, et al., High-temperature tribological and oxidation behaviour of PTAW-deposited NiCrBSi coating in steel-on-coating contact up to 800 °C, Tribol. Int. 215 (2026) 111503, https://doi.org/10.1016/j.triboint.2025.111503.
[18] M. Yin, et al., Microstructure, mechanical and tribological behavior of CrHfNbTaTiCxNy high-entropy carbonitride coatings prepared by double glow plasma alloy, Wear 523 (2023) 204751, https://doi.org/10.1016/j.wear.2023.204751.
[19] J. Zheng, et al., AlCrNiTiZr)Nx high-entropy nitride coatings with enhanced hardness via tailoring N2 flow rates for anti-wear applications, J. Vac. Sci. & Technol. A 41 (5) (Jul. 2023) 053404, https://doi.org/10.1116/6.0002837.
[20] T.J. Harrington, et al., Phase stability and mechanical properties of novel high entropy transition metal carbides, Acta Mater. 166 (Mar. 2019) 271–280, https://doi.org/10.1016/j.actamat.2018.12.054.
[21] A. Kretschmer, H. Rojacz, E. Badisch, P. Polcik, P.H. Mayrhofer, High-temperature tribological behavior of high-entropy sublattice oxide, nitride, and diboride coatings, Surf. Coat. Technol. 489 (2024) 131037, https://doi.org/10.1016/j.surfcoat.2024.131037.
[22] H. Yu, et al., High-temperature oxidation resistance and wear properties of functionally graded CrHfNbTaTiN high-entropy nitride coating on Ti alloy, Appl. Surf. Sci. 680 (2025) 161474, https://doi.org/10.1016/j.apsusc.2024.161474.
[23] L. Backman, J. Gild, M. Qin, J. Luo, E.J. Opila, Composition dependence of oxidation resistance in high entropy ultra-high temperature ceramics, Open. Ceram. 18 (2024) 100563, https://doi.org/10.1016/j.oceram.2024.100563.
[24] W.-L. Lo, S.-Y. Hsu, Y.-C. Lin, S.-Y. Tsai, Y.-T. Lai, J.-G. Duh, Improvement of high entropy alloy nitride coatings (AlCrNbSiTiMo)N on mechanical and high temperature tribological properties by tuning substrate bias, Surf. Coat. Technol. 401 (2020) 126247, https://doi.org/10.1016/j.surfcoat.2020.126247.
[25] R. Chen, H. An, J. Zhan, S. Li, A. Mao, H. Wen, High-temperature oxidation behavior of high entropy carbide (TaNbTiV)C in atmospheres with different oxygen contents, Ceram. Int. 50 (21) (2024) 43165–43170, https://doi.org/10.1016/j.ceramint.2024.08.167.
[26] R. Djenadic, et al., Multicomponent equiatomic rare earth oxides, Mater. Res. Lett. 5 (2) (Mar. 2017) 102–109, https://doi.org/10.1080/21663831.2016.1220433.
[27] H. Vakilifard, et al., High Entropy Oxides as Promising Materials for Thermal Barrier Topcoats: A Review, J. Therm. Spray. Technol. 33 (2) (2024) 447–470, https://doi.org/10.1007/s11666-024-01744-0.
[28] F. Li, L. Zhou, J.-X. Liu, Y. Liang, G.-J. Zhang, High-entropy pyrochlores with low thermal conductivity for thermal barrier coating materials, J. Adv. Ceram. 8 (4) (2019) 576–582, https://doi.org/10.1007/s40145-019-0342-4.
[29] S. Jiang, et al., A new class of high-entropy perovskite oxides, Scr. Mater. 142 (2018) 116–120, https://doi.org/10.1016/j.scriptamat.2017.08.040.
[30] L. Xu, H. Wang, L. Su, D. Lu, K. Peng, H. Gao, A new class of high-entropy fluorite oxides with tunable expansion coefficients, low thermal conductivity and exceptional sintering resistance, J. Eur. Ceram. Soc. 41 (13) (2021) 6670–6676, https://doi.org/10.1016/j.jeurceramsoc.2021.05.043.
[31] D. LIU, B. SHI, L. GENG, Y. WANG, B. XU, Y. CHEN, High-entropy rare-earth zirconate ceramics with low thermal conductivity for advanced thermal-barrier coatings, J. Adv. Ceram. 11 (6) (2022) 961–973, https://doi.org/10.1007/s40145-022-0589-z.
[32] G. Du, et al., Situ Synthesis and Wide-Temperature Tribological Properties of Biphasic Structure High-Entropy (Mg 1/6 Ni 1/6 Co 1/6 Cu 1/6 Zn 1/6 Al 1/6) 3 O 4 Ceramics, Langmuir 41 (Jan. 2025), https://doi.org/10.1021/acs.langmuir.5c04475.
[33] Z. Zhao, H. Xiang, F.-Z. Dai, Z. Peng, Y. Zhou, La0.2Ce0.2Nd0.2Sm0.2Eu0.2) 2Zr2O7: A novel high-entropy ceramic with low thermal conductivity and sluggish grain growth rate, J. Mater. Sci. Technol. 35 (11) (2019) 2647–2651, https://doi.org/10.1016/j.jmst.2019.05.054.
[34] H. Vakilifard, F. Ben Ettouil, R.S. Lima, M.D. Pugh, C. Moreau, Isothermal Oxidation Performance of High-Entropy Zirconate as an Advanced Topcoat for Thermal Barrier Coatings, J. Therm. Spray. Technol. (2025), https://doi.org/10.1007/s11666-025-02103-3.
[35] H. Junjie, H. Guo, L. Jing, T. Jingchao, New class of high-entropy defect fluorite oxides RE2(Ce0.2Zr0.2Hf0.2Sn0.2Ti0.2)2O7 (RE = Y, Ho, Er, or Yb) as promising thermal barrier coatings, J. Eur. Ceram. Soc. 41 (12) (2021) 6080–6086, https://doi.org/10.1016/j.jeurceramsoc.2021.05.044.

[36] X. Zhang, Y. Wu, Y. Ma, L. Chen, H. Li, High-entropy (MgCoNiCuZn)O5 ceramic coatings by sol-gel method: Tribological and protective properties over a wide temperature range, Tribol. Int. 218 (2026) 111754, https://doi.org/10.1016/j.triboint.2026.111754.
[37] A. Kretschmer, H. Rojacz, E. Badisch, P. Polcik, P.H. Mayrhofer, High-temperature tribological behavior of high-entropy sublattice oxide, nitride, and diboride coatings, Surf. Coat. Technol. 489 (Aug. 2024), https://doi.org/10.1016/j.surfcoat.2024.131037.
[38] D. Tejero-Martin, C. Bennett, T. Hussain, A review on environmental barrier coatings: History, current state of the art and future developments, J. Eur. Ceram. Soc. 41 (3) (2021) 1747–1768, https://doi.org/10.1016/j.jeurceramsoc.2020.10.057.
[39] W. Zhang, S. Yamashita, H. Kita, Progress in tribological research of SiC ceramics in unlubricated sliding-A review, Mater. Des. 190 (2020) 108528, https://doi.org/10.1016/j.matdes.2020.108528.
[40] M.-L. Cliche, A.R. Mayer, G. Cha, S. Christiansen, P. Stoyanov, High-temperature tribological performance of superalloys and silicon carbide: exploring ceramic materials for tribological interfaces in next-generation gas turbines, Wear 578–579 (2025) 206220, https://doi.org/10.1016/j.wear.2025.206220.
[41] M. Lavella, D. Botto, Fretting wear of T800 coating in aero-engine applications. Proceedings of the ASME Turbo Expo, American Society of Mechanical Engineers (ASME), 2020, https://doi.org/10.1115/GT2020-15608.
[42] R. Kumar, I. Hussainova, R. Rahmani, M. Antonov, Solid Lubrication at High-Temperatures—A Review, MDPI, Mar. 01, 2022, https://doi.org/10.3390/ma15051695.
[43] X. He, Z. Wang, Y. Yan, K. Zheng, Q. Bai, Role of Surface Morphology Evolution in the Tribological Behavior of Superalloy Under High-Temperature Fretting, Materials 18 (10) (2025), https://doi.org/10.3390/ma18102350.
[44] W. Huai, C. Zhang, S. Wen, Graphite-based solid lubricant for high-temperature lubrication, Friction 9 (6) (Dec. 2021) 1660–1672, https://doi.org/10.1007/s40544-020-0456-2.
[45] T. König, E. Wolf, P. Daum, D. Kürten, A. Kailer, M. Dienwiebel, Influencing factors on high temperature tribology, Wear 566–567 (2025) 205758, https://doi.org/10.1016/j.wear.2025.205758.
[46] S. Zhang, Z. Wang, W. Lin, H. Guo, Research Progress on Tribological Properties of High-Entropy Alloys, Lubricants 13 (8) (2025), https://doi.org/10.3390/lubricants13080342.
[47] P. Hutterer, M. Lepple, Influence of composition on structural evolution of high-entropy zirconates—cationic radius ratio and atomic size difference, J. Am. Ceram. Soc. 106 (2) (Feb. 2023) 1547–1560, https://doi.org/10.1111/jace.18832.
[48] S.M. Aouadi, et al., Adaptive Mo 2N/MoS 2/Ag tribological nanocomposite coatings for aerospace applications, Tribol. Lett. 29 (2) (Feb. 2008) 95–103, https://doi.org/10.1007/s11249-007-9286-x.
[49] E.E. Balić, T.A. Blanchet, Thrust-washer tribological evaluation of PS304 coatings against Rene 41, Wear 259 (7) (2005) 876–881, https://doi.org/10.1016/j.wear.2005.02.051.
[50] J.H. Ouyang, Y.F. Li, Y.Z. Zhang, Y.M. Wang, Y.J. Wang, High-Temperature Solid Lubricants and Self-Lubricating Composites: A Critical Review, MDPI, Aug. 01, 2022, https://doi.org/10.3390/lubricants10080177.
[51] Z. Zhang, et al., Spinel oxide enables high-temperature self-lubrication in superalloys, Nat. Commun. 15 (1) (Dec. 2024), https://doi.org/10.1038/s41467-024-54482-w.
[52] A. Roy, et al., Microstructural evolution and tribological behavior of suspension plasma sprayed CuO as high-temperature lubricious coatings, Wear 524–525 (2023) 204874, https://doi.org/10.1016/j.wear.2023.204874.
[53] A. Roy, et al., Friction and wear behavior of suspension plasma sprayed tantalum oxide coatings at elevated temperatures, Surf. Coat. Technol. 452 (2023) 129097, https://doi.org/10.1016/j.surfcoat.2022.129097.
[54] J. Li, et al., Carbon-deficient high-entropy (Zr0.17Nb0.2Ta0.2Mo0.2W0.2)C0.89: A potential high temperature and vacuum wear-resistant material, Mater. Des. 226 (Feb. 2023), https://doi.org/10.1016/j.matdes.2023.111680.
[55] D. Guo, et al., High-temperature tribological characteristics and lubrication mechanisms of NiCrAlY-MoO3/CoO composite coatings: An experimental and DFT computation study, Surf. Coat. Technol. 496 (2025) 131701, https://doi.org/10.1016/j.surfcoat.2024.131701.
[56] Y. Wang, X. Shao, J. Liu, X. Hu, X. He, G. Deng, Difference in High-Temperature Tribological Performance of Oxide/Ag-MoS2-Based Composites, Lubricants 12 (10) (2024), https://doi.org/10.3390/lubricants12100360.
[57] J. Xie, et al., Controlling the porosity to enhance the high-temperature tribological performance of plasma-sprayed NiCr–Cr3C2–BaF2/CaF2 coating by adopting axial feeding, J. Mater. Res. Technol. 36 (2025) 2577–2588, https://doi.org/10.1016/j.jmrt.2025.03.273.
[58] B.R. Marple, R.S. Lima, C. Moreau, S.E. Kruger, L. Xie, M.R. Dorfman, Yttria-Stabilized Zirconia Thermal Barriers Sprayed Using N2-H2 and Ar-H2 Plasmas: Influence of Processing and Heat Treatment on Coating Properties, J. Therm. Spray. Technol. 16 (5) (2007) 791–797, https://doi.org/10.1007/s11666-007-9093-9.
[59] J.F. Bisson, M. Lamontagne, C. Moreau, L. Pouliot, J. Blain, F. Nadeau, Ensemble In-Flight, Part. Diagn. Therm. Spray. Cond. (2001), https://doi.org/10.31399/asm.cp.itsc2001p0705.
[60] A. Kulkarni, et al., Studies of the microstructure and properties of dense ceramic coatings produced by high-velocity oxygen-fuel combustion spraying, Materials Science Engineering A 369 (1) (2004) 124–137, https://doi.org/10.1016/j.msea.2003.10.295.
[61] Kenneth C. Ludema and Ajayi Layo, Friction, Wear, Lubrication A Textbook in Tribology, Second Edition. 2018.
[62] Holmberg Kenneth, Matthews Allan, Coatings Tribology Properties, Mechanisms, Techniques and Applications in Surface Engineering, 2nd Edition., 56, Elsevier, 2009.
[63] K. Derelizade, F. Venturi, R.G. Wellman, A. Kholobysov, T. Hussain, Wear performance of graphene nano platelets incorporated WC-Co coatings deposited by hybrid high velocity oxy fuel thermal spray, Wear 482–483 (2021) 203974, https://doi.org/10.1016/j.wear.2021.203974.
[64] P. Patel, et al., Microstructural and Tribological Behavior of Thermal Spray CrMnFeCoNi High Entropy Alloy Coatings, J. Therm. Spray. Technol. 31 (Mar. 2022) 1285–1301, https://doi.org/10.1007/s11666-022-01350-y.
[65] L. Xin, Y. Han, L. Ling, W. Zhang, Y. Lu, T. Shoji, The Evolution of Fretting Wear Behavior and Damage Mechanism in Alloy 690TT with Cycle Number, Materials 13 (10) (2020), https://doi.org/10.3390/ma13102417.
[66] S.R. Soria, A. Tolley, A. Yawny, A study of debris and wear damage resulting from fretting of Incoloy 800 steam generator tubes against AISI Type 304 stainless steel, Wear 368–369 (2016) 219–229, https://doi.org/10.1016/j.wear.2016.09.022.
[67] M. Godet, Third-bodies in tribology, Wear 136 (1) (1990) 29–45, https://doi.org/10.1016/0043-1648(90)90070-Q.
[68] I.L. Singer, How Third-Body Processes Affect Friction and Wear, MRS Bull. 23 (6) (1998) 37–40, https://doi.org/10.1557/S088376940003061X.
[69] A.M. Kirk, P.H. Shipway, W. Sun, C.J. Bennett, Debris development in fretting contacts – Debris particles and debris beds, Tribol. Int. 149 (2020) 105592, https://doi.org/10.1016/j.triboint.2019.01.051.
[70] D. Chen, C. Dambra, M. Dorfman, Deposition, Microstructure and Thermal Cycling Performance of Strain-Tolerant Thermal Barrier Coatings, J. Therm. Spray. Technol. 32 (4) (2023) 1108–1114, https://doi.org/10.1007/s11666-022-01516-8.
[71] P. Blau, *Friction Science and Technology: From Concepts to Applications, Second Edition*. 2008. doi: 10.1201/9781420054101.
[72] X. Jin, P.H. Shipway, W. Sun, The Role of Temperature and Frequency on Fretting Wear of a Like-on-Like Stainless Steel Contact, Tribol. Lett. 65 (3) (2017) 77, https://doi.org/10.1007/s11249-017-0858-0.
[73] F.H. Stott, High-temperature sliding wear of metals, Tribol. Int. 35 (8) (2002) 489–495, https://doi.org/10.1016/S0301-679X(02)00041-5.
[74] I.A. Inman, P.K. Datta, H.L. Du, J.S. Burnell-Gray, S. Pierzgalski, Q. Luo, Studies of high temperature sliding wear of metallic dissimilar interfaces, Tribol. Int. 38 (9) (2005) 812–823, https://doi.org/10.1016/j.triboint.2005.02.007.
[75] Y. Berthier, L. Vincent, M. Godet, Velocity accommodation in fretting, Wear 125 (1) (1988) 25–38, https://doi.org/10.1016/0043-1648(88)90191-3.